

Article

# Numerical Analysis and Characterization of Surface Pressure Fluctuations of High-Speed Trains Using Wavenumber–Frequency Analysis

Songjune Lee <sup>1</sup>, Cheolung Cheong <sup>1,\*</sup> , Jaehwan Kim <sup>2</sup> and Byung-hee Kim <sup>2</sup>

<sup>1</sup> School of Mechanical Engineering, Pusan National University, Busan 46241, Korea; sjlee@pusan.ac.kr

<sup>2</sup> Applied Technology Research Team, Hyundai Rotem Company, 37 Cheoldobangmulgwan-ro, Uiwang-si Gyeonggi-do 16082, Korea; jhkim131@hyundai-rotem.co.kr (J.K.); bhkim@hyundai-rotem.co.kr (B.-h.K.)

\* Correspondence: ccheong@pusan.ac.kr; Tel.: +82-(0)51-510-2311

Received: 8 October 2019; Accepted: 14 November 2019; Published: 15 November 2019



**Abstract:** The high-speed train interior noise induced by the exterior flow field is one of the critical issues for product developers to consider during design. The reliable numerical prediction of noise in a passenger cabin due to exterior flow requires the decomposition of surface pressure fluctuations into the hydrodynamic (incompressible) and the acoustic (compressible) components, as well as the accurate computation of the near aeroacoustic field, since the transmission characteristics of incompressible and compressible pressure waves through the wall panel of the cabin are quite different from each other. In this paper, a systematic numerical methodology is presented to obtain separate incompressible and compressible surface pressure fields in the wavenumber–frequency and space–time domains. First, large eddy simulation techniques were employed to predict the exterior flow field, including a highly-resolved acoustic near-field, around a high-speed train running at the speed of 300 km/h in an open field. Pressure fluctuations on the train surface were then decomposed into incompressible and compressible fluctuations using the wavenumber–frequency analysis. Finally, the separated incompressible and compressible surface pressure fields were obtained from the inverse Fourier transform of the wavenumber–frequency spectrum. The current method was illustratively applied to the high-speed train HEMU-430X running at a speed of 300 km/h in an open field. The results showed that the separate incompressible and compressible surface pressure fields in the time–space domain could be obtained together with the associated aerodynamic source mechanism. The power levels due to each pressure field were also estimated, and these can be directly used for interior noise prediction.

**Keywords:** high-speed train; aerodynamic noise; wavenumber–frequency analysis; hydrodynamic pressure; acoustic pressure

## 1. Introduction

High-speed trains have been competitively developed around the world since the first line was launched in Japan in 1964. The competition accelerated after the running speed of the French high-speed train TGV V150 exceeded 574.8 km/h. Many relevant studies have been carried out by worldwide manufacturers seeking to develop the fastest train, because it manifests technological superiority over others. However, as the running speed of high-speed trains increased, noise emissions also inevitably increased. Modern high-speed trains have two main distinctive noise sources: rolling noise caused by the interaction between wheels and rail, and aerodynamic noise caused by flow around the train [1]. According to related studies, the sound power due to rolling noise is known to increase in proportion with the third power of train speed  $V$ . On the other hand, the sound power of aerodynamic noise

increases with  $V^6$  and  $V^8$  for dipole and quadrupole sources, respectively [1]. Therefore, the relative contribution of aerodynamic noise becomes more important as the travel speed of the train increases. It has been reported that aerodynamic noise sources begin to contribute more to the overall noise levels as the travel speed of the train exceeds 300 km/h [2].

Recently, several studies [2–6] were carried out on the aerodynamic noise of high-speed trains. Various methods such as full-scale measurements, scaled-model tests in a wind tunnel, and numerical approaches were used, and the common results were that the first bogie, the first pantograph, and the first intercoach spacing were the aerodynamic sources contributing most to the radiated noise field. However, these studies used a simplified external body model or only a single part of a train, and focused only on externally radiated noise.

The ultimate goal of this paper was to develop reliable, systematic numerical methods for the prediction of interior cabin noise of a high-speed train, which is one of the critical issues for the product developers. However, the fact that the interior cabin noise is directly caused only by the vibration of the cabin body structures made it more challenging to understand and model the relevant physical mechanism. The vibration of cabin body structure can be induced by external flow, including the acoustic field, as well as by the interaction between wheels and rail. The former and the latter can be called flow-borne and structure-borne vibrations, respectively. However, the external flow fluctuations consist of incompressible and compressible waves. The former is sometimes called hydrodynamic fluctuation or pseudo-sound, and the latter is called an acoustic wave. Again, compressible waves can be generated by the structural vibration and/or aerodynamic noise sources. This fact implies that the accurate flow field predictions including the aerodynamic noise sources and their corresponding acoustic waves are essential for the accurate prediction of interior cabin noise of a high-speed train, under the assumption that the aerodynamic noise is more dominant in the overall noise of a high-speed train.

In the present study, as a first step for achieving the ultimate goal, the systematic numerical methodology presented was used to obtain separate incompressible and compressible surface pressure fields in the frequency–wavenumber and time–space domains. First, LES (large eddy simulation) techniques were employed to predict the flow field, including the acoustic field, around a high-speed train running in an open field. Second, pressure fluctuations on the train surface were decomposed into incompressible and compressible ones using wavenumber–frequency analysis. The separation is based on the physical fact that the wave speeds of incompressible and compressible pressure waves are different from each other. Finally, the separated incompressible and compressible surface pressure fields in the space–time domain were obtained from the inverse Fourier transform of the wavenumber–frequency spectrum. The current method was illustratively applied to the high-speed train HEMU-430X running at a speed of 300 km/h in an open field.

## 2. Numerical Methods and Target Model

### 2.1. Large Eddy Simulation

In this section, LES is briefly introduced. LES with the Smagorinsky–Lilly model was used to solve the governing equation predicting the external flow and acoustic field around a train body. LES directly computes only large eddies, and hence a low-pass spatial filter was applied to the conservation equations to formulate the unsteady governing equations for large scale motion. The three-dimensional, compressible, unsteady LES governing equations with the turbulent viscosity of the Smagorinsky–Lilly model can be written in the forms below:

$$\begin{aligned} \frac{\partial \bar{\rho}}{\partial t} + \frac{\partial}{\partial x_i} (\bar{\rho} \bar{u}_i) &= 0 \\ \frac{\partial}{\partial t} (\bar{\rho} \bar{u}_i) + \frac{\partial}{\partial x_j} (\bar{\rho} \bar{u}_i \bar{u}_j) &= \frac{\partial}{\partial x_i} (\bar{\sigma}_{ij}) - \frac{\partial \bar{p}}{\partial x_i} - \frac{\partial \tau_{ij}}{\partial x_j} \\ \frac{\partial \bar{\rho} \bar{h}_s}{\partial t} + \frac{\partial \bar{\rho} \bar{u}_i \bar{h}_s}{\partial x_i} - \frac{\partial \bar{p}}{\partial t} - \bar{u}_j \frac{\partial \bar{p}}{\partial x_i} - \frac{\partial}{\partial x_i} \left( \lambda \frac{\partial \bar{T}}{\partial x_i} \right) &= - \frac{\partial}{\partial x_j} \left[ \rho \left( \bar{u}_i \bar{h}_s - \bar{u}_i \bar{h}_s \right) \right] \end{aligned} \quad (1)$$

$$\mu_t = \rho L_s^2 \left| \bar{S} \right| \text{ where, } \left| \bar{S} \right| = \sqrt{2\bar{S}_{ij}\bar{S}_{ij}} \tag{2}$$

where  $\bar{S}_{ij}$  is the rate of the strain tensor and  $L_s$  is the mixing length, which represents the length scale of turbulence components smaller than the grid size. These terms can be written in the following form.

$$\bar{S}_{ij} = \frac{1}{2} \left( \frac{\partial \bar{u}_i}{\partial \bar{x}_j} + \frac{\partial \bar{u}_j}{\partial \bar{x}_i} \right) \tag{3}$$

$$L_s = \min(\kappa d, C_s \Delta), \Delta = V^{1/3} \tag{4}$$

where  $\kappa$  is the von Karman constant,  $d$  is the distance to the nearest wall,  $C_s$  is the Smagorinsky constant, and  $\Delta$  is the local grid size. The discretization methods are listed in Table 1. The LES was numerically realized using the commercial software ANSYS Fluent (version: 18.0).

**Table 1.** Discretization schemes of governing equations.

Equations	Discretization Method
Pressure	Second order
Momentum	Bounded central differencing
Energy	Second order upwind
Transient formulation	Second order implicit

### 2.2. Wavenumber–Frequency Analysis

The wavenumber–frequency diagram of surface pressure fluctuation can be obtained from the three-dimensional Fourier transform of the surface pressure in the space–time domain. It shows the distribution of the magnitude of the specific wave component in terms of wavenumber  $k$  and frequency  $\omega$  in the wavenumber–frequency domain. One of the advantages of using the wavenumber–frequency spectrum instead of the space–time diagram is that the phase speed of the specific wave component constituting surface pressure fluctuations in the space–time domain can be determined. The phase speed  $v_p = \omega/k$  can be used as a criterion to decompose the surface pressure fluctuation into its incompressible and compressible components. The former is convected at the velocity proportional to mean flow velocity  $U_0$ , and the latter does so at the vector sum of mean flow velocity and the sound speed  $c_0$ . The spatial–temporal pressure field on a train wall can be characterized using the correlation function.

$$R(\mathbf{x}; \boldsymbol{\xi}, \tau) = \langle p'(\mathbf{x}, t) \cdot p'(\mathbf{x} + \boldsymbol{\xi}, t + \tau) \rangle \tag{5}$$

where  $\boldsymbol{\xi}$  is the distance vector,  $\tau$  is the time delay, and  $p'$  is the perturbed pressure. The correlation function of the spatial–temporal pressure field can be converted to the wavenumber–frequency domain using a Fourier transform. The Fourier transform from the space–time domain to the wavenumber–frequency domain is written as

$$S(\mathbf{k}, \omega) = \int_{-\infty}^{\infty} \int_{-\infty}^{\infty} \int_{-\infty}^{\infty} R(\boldsymbol{\xi}, \tau) e^{-i(\mathbf{k}\boldsymbol{\xi} + \omega\tau)} d\xi_1 d\xi_2 d\tau \tag{6}$$

The power spectral density (PSD) of the wall pressure fluctuations can be estimated using the periodogram method in the following form:

$$S(\mathbf{k}, \omega) = \lim_{T, L_1, L_2 \rightarrow \infty} \frac{1}{L_1} \frac{1}{L_2} \frac{1}{T} \langle \hat{p}_{L,T}(\mathbf{k}, \omega) \cdot \hat{p}_{L,T}^*(\mathbf{k}, \omega) \rangle \tag{7}$$

where

$$\hat{p}_{L,T}(\mathbf{k}, \omega) = \int_{-T/2}^{T/2} \int_{-L_1/2}^{L_1/2} \int_{-L_2/2}^{L_2/2} p'(x, t) e^{-i(kx + \omega t)} dx_1 dx_2 dt \tag{8}$$

and  $\hat{p}_{L,T}^*$  is a complex conjugate of  $\hat{p}_{L,T}$ . In Equation (8),  $L_1$ , and  $L_2$  are the length of space domain in each direction, respectively, and  $T$  is the time period. Finally, the three-dimensional discrete Fourier transform equation used to obtain the three-dimensional averaged modified periodogram can be written in the following form [7,8].

$$S_{m,n,o} = S(m\Delta f, n\Delta k_{x_1}, o\Delta k_{x_2}) = \frac{\Delta x_1 \Delta x_2}{N_t N_{x_1} N_{x_2} F_s} \left| \sum_{k=0}^{N_t-1} \sum_{l=0}^{N_{x_1}-1} \sum_{j=0}^{N_{x_2}-1} w_{klj} P_{klj} e^{-2i\pi(\frac{km}{N_t} - \frac{nl}{N_{x_1}} - \frac{oj}{N_{x_2}})} \right|^2 / \frac{1}{N_t N_{x_1} N_{x_2}} \sum_{k=0}^{N_t-1} \sum_{l=0}^{N_{x_1}-1} \sum_{j=0}^{N_{x_2}-1} |w_{klj}|^2 \tag{9}$$

where  $w_{klj}$  is a discretized Hanning window.

In the three-dimensional periodogram, the incompressible and compressible parts can be separated by using the slanted Dirac cone defined as

$$\omega = c_0 \sqrt{k_{x_1}^2 + k_{x_2}^2} + k_{x_1} U_0 \tag{10}$$

where  $U_0$  is free stream velocity. The acoustic wavenumber  $k_a$  which is used as the criteria to distinguish between the acoustic and convection components can be obtained by dividing both sides of Equation (10) with the speed of sound, giving

$$k_a = \omega / c_0 = \sqrt{k_{x_1}^2 + k_{x_2}^2} + k_{x_1} M \tag{11}$$

where  $M$  is the Mach number. Components that satisfy the unequal equation of  $|k| \leq k_a$  are then classified as either compressible waves or as incompressible ones.

Figure 1 illustrates the slanted Dirac cone for the case where  $U_0 = 300$  km/h and  $c_0 = 343$  m/s.

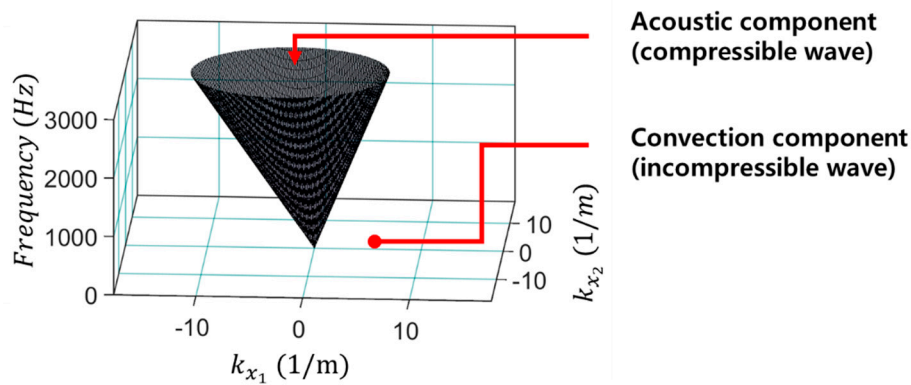


**Figure 1.** Illustrative slanted Dirac cone separating incompressible and compressible parts in the three-dimensional periodogram:  $U_0 = 300$  km/h and  $c_0 = 343$  m/s.

### 2.3. Target Model and Details on Simulation

Figure 2 shows the entire computational domain with the related dimensions and the applied boundary conditions. The speed of the train was set as a velocity inlet boundary condition. The atmospheric pressure was used as a pressure outlet boundary condition. The non-reflective boundary condition was also applied for the inlet and outlet regions to capture the aerodynamic noise without non-physical reflection off the boundaries. Pressure far-field boundary conditions were applied on the upper and two side boundary surfaces. The non-slip wall boundary conditions were

applied on the surface of HEMU. Moving wall boundary conditions were applied on the ground and the rails. The detailed boundary conditions with their specified values are listed in Table 2.

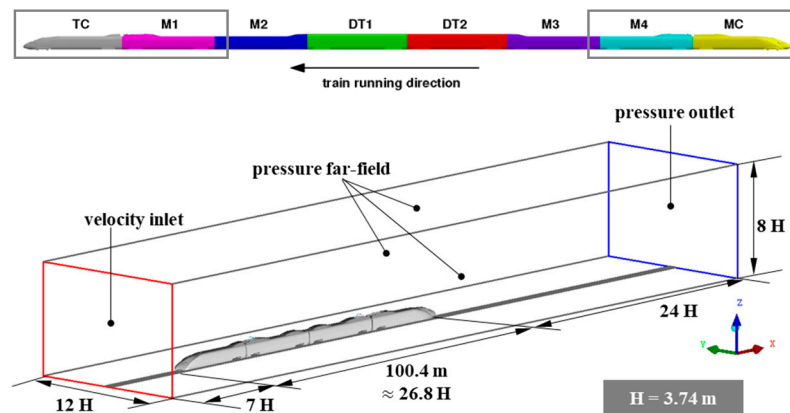


Figure 2. Computational domain for open field case (1H: height of train).

Table 2. Details on boundary setting for the open field case.

Boundary	Setting	Remarks
Inlet boundary	Velocity inlet	83.33 m/s (300 km/h), non-reflecting
Outlet boundary	Pressure outlet	101,325 Pa, non-reflecting
Side and upper boundary	Pressure far field	101,325 Pa, Ma = 0.24
Ground boundary	Moving wall	83.33 m/s
HEMU wall	No-slip wall	
Rail wall	Moving wall	

Figure 3 shows the CAD model of the targeted train and its main parts. The targeted train was HEMU-430X (High-speed Electric Multiple Unit 430 km/h experimental), which is under development as a next-generation Korean high-speed train, for which the maximum speed has been recorded as 430 km/h. It consists of eight coaches including double-deck carriages, as shown in Figure 2. However, for simplicity but without losing the main aerodynamic source mechanisms, only four coaches which are a trailer coach (TC), first motor coach (M1), fourth motor coach (M4), and the last motor coach (MC) were considered in the current study. The detailed, full-scale geometry including eight bogies, two pantographs, one wiper, and three intercoach spaces was modeled to capture the essential aerodynamic noise source mechanisms. Figure 4 shows the grid description for the computational domain. The computational mesh was composed of about 310 million cells using fluent meshing. Tetrahedral and hexacore cells were used together with five layers of prismatic elements near the wall surface.

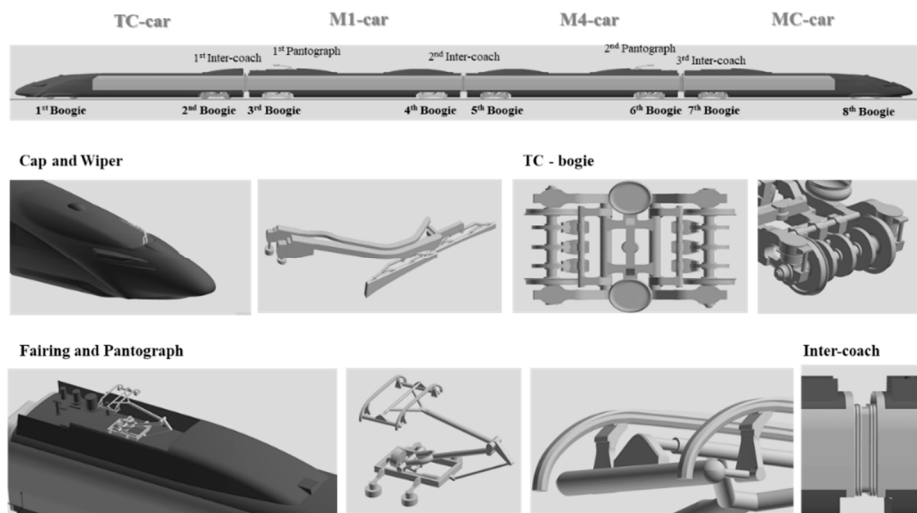


Figure 3. Target train model (HEMU-430X) and its main parts.

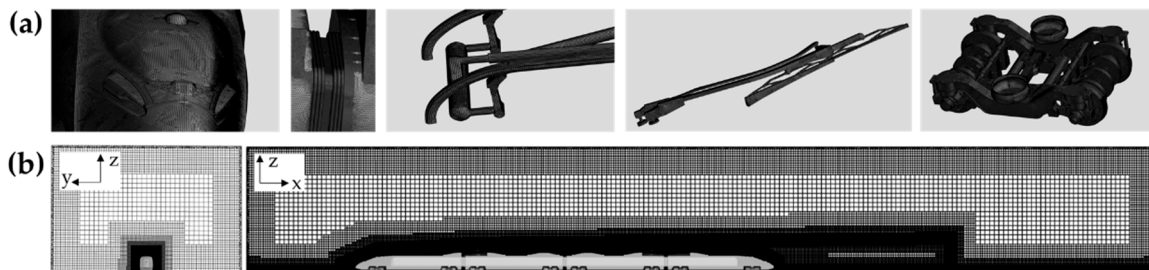


Figure 4. Grid description of target model and fluid region: (a) surface meshes of its main parts; (b) volume meshes in the y–z and x–z planes.

### 3. Validation of Numerical Methods

To ensure the validity of current numerical methods, the aerodynamic drag of the high-speed train was computed and compared with the results reported in previous studies. Aerodynamic drag was compared in terms of a non-dimensional drag coefficient,  $C_d$ , defined in the following form.

$$C_d = \frac{D}{\frac{1}{2}\rho u^2 S} \tag{12}$$

where  $D$  is the drag force,  $\rho$  is the air density,  $u$  is the freestream velocity, and  $S$  is the reference cross-sectional area. The air density and the reference area were  $1.225 \text{ kg/m}^3$  and  $11.59 \text{ m}^2$ , respectively. Kwon [9] calculated the aerodynamic drag of a Korean high-speed train using the coasting test method. In Table 3, the aerodynamic drag ( $C_d$ ) of HEMU-430X predicted in the present study is compared with that calculated by Kwon [9]. The former was 0.612 and the latter was 0.900. Considering the fact that the current train consisted of four coaches and the experimental one consisted of six coaches, there was good agreement between two results in that the drag coefficients for one coach were 0.153 and 0.15, respectively.

Table 3. Drag coefficient of HEMU-430X.

	Train Formation	$C_d$
H. Kwon (from coasting test)	TC + 4M + MC (6 coaches)	0.900
Present study	TC + 2M + MC (4 coaches)	0.612

#### 4. Unsteady Flow and Analysis

In this section, the numerical simulation results are presented with the main aerodynamic noise generation mechanism of a high-speed train.

##### 4.1. Overall Flow Characteristics

Figure 5 shows the computed instantaneous iso-surfaces of the Q-criterion. It can be observed that strong coherent vortex structures were generated from the bogie fairing, the headlamp, and the wiper in the first coach. Large vortices were created and propagated from the first bogie, the first pantograph, and the intercoach space, which are known to be dominant aerodynamic noise sources. Attached flow generally existed on the TC car (first coach), but the strong separated flows caused by the first pantograph covered the remaining coaches downstream. Figure 6 shows the instantaneous iso-contours of the velocity magnitudes at the centered cross-sectional plane. It can be seen that significant velocity reduction was induced in the underbody. It was also shown that strong separated flows covered the downstream coaches behind the TC car.

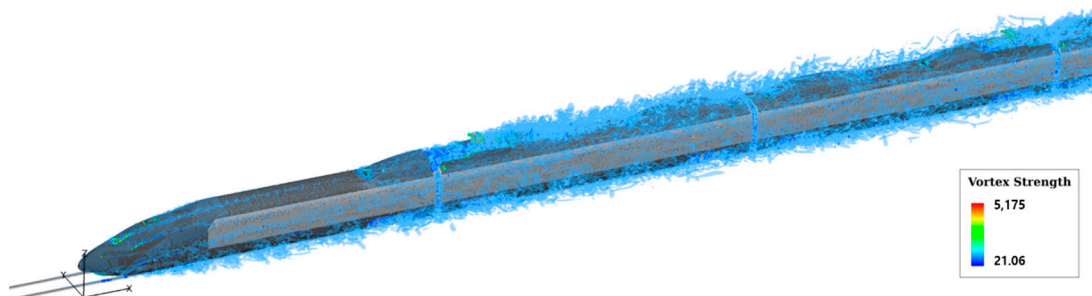


**Figure 5.** Instantaneous iso-surfaces of Q-criterion ( $=3,000$ ) and vortex core with its strength of open field case.

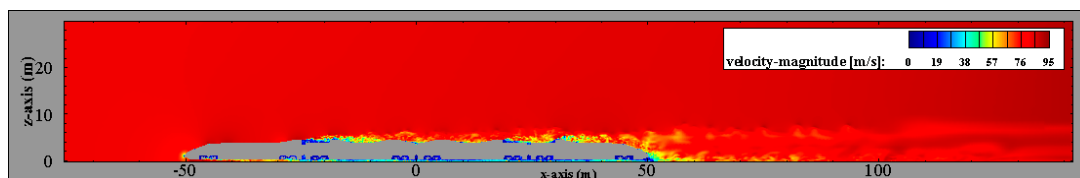


**Figure 6.** Instantaneous velocity magnitude contour of open field case.

Figure 7 shows the instantaneous iso-contours of pressure on the central vertical cross-sectional plane and the horizontal plane. It was seen that the compressible acoustic pressure waves were propagated from the train coaches. It was identified that the main aerodynamic sources were the bogies, pantographs, intercoach gabs, and roof fairings. The more detailed aerodynamic source generation mechanisms in these sources are described in the following three sections.

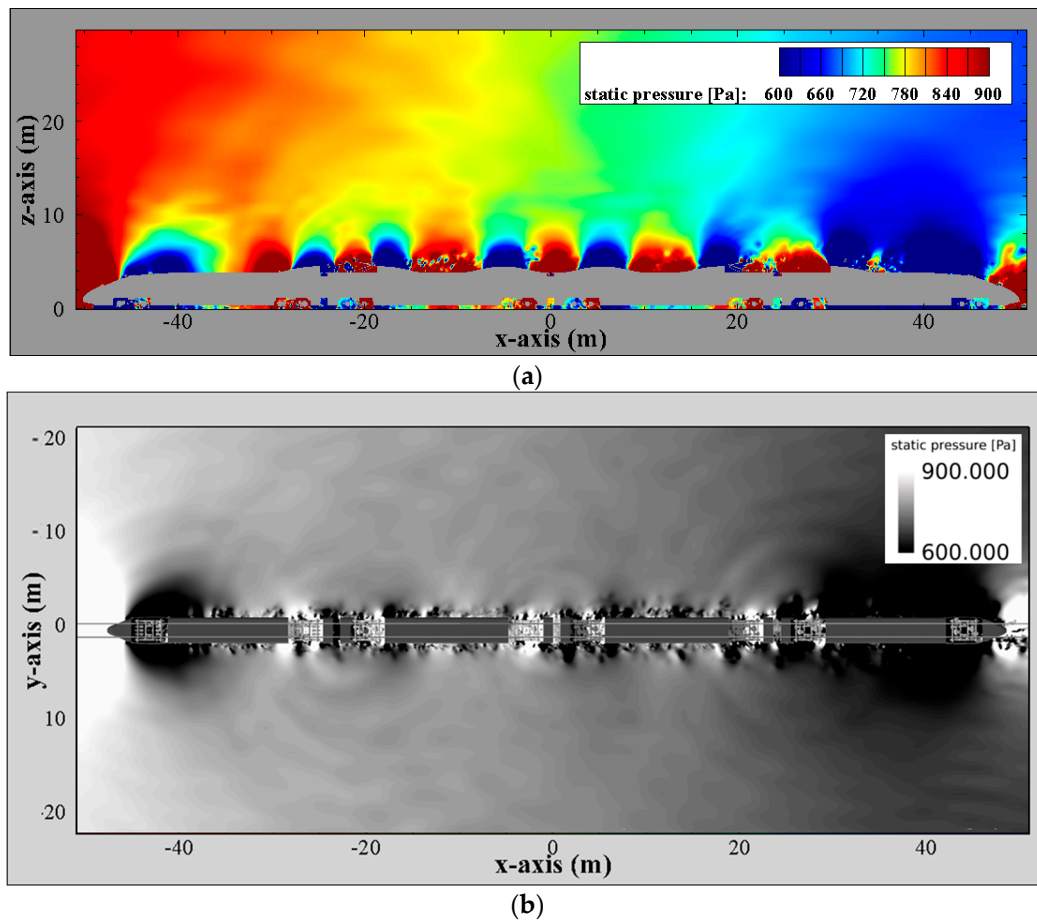


**Figure 7.** Instantaneous static pressure contour: (a) x–z plane,  $y = 0$  m; (b) x–y plane,  $z = 1$  m.

#### 4.2. Bogie

Figure 8 shows two bogie models attached to the trailer coach (TC) and the motor coach (MC), respectively, which commonly consists of a bogie frame, wheelset, break unit, and secondary suspension between the body of the coach and bogie. The main motor and gear unit are installed in the MC bogie. Although the noise generated by the pantograph has received the most attention, aerodynamic noise produced from the bogie region has been estimated to be higher by around 15 dB than that from the pantograph in terms of the overall noise level of the whole train [10]. Figure 9 shows the instantaneous iso-contours of vorticity magnitudes at the cross-sectional planes of  $y = -0.6$  m,  $y = 0$  m, and  $y = 0.6$  m of the first and eighth bogies, respectively. It was shown that flow separation occurred at the front edge and formed vortices. The vortices were convected downstream, first hit the front wheelset and then induced wake vortices again. The wake vortices formed behind the front wheelset were convected inside the bogie region and developed complex, unsteady flow around the brake units and the rear wheelset. Figure 10 shows the instantaneous surface pressure contours of the first and eighth bogies. The flow impact on the first bogie was more significant than the flow impact on the eighth bogie, implying that a higher dipolar noise was generated on the first bogie.

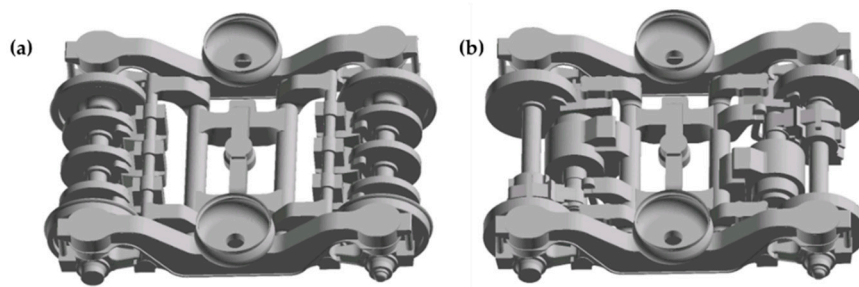


Figure 8. Simplified bogie models: (a) TC bogie; (b) MC bogie.

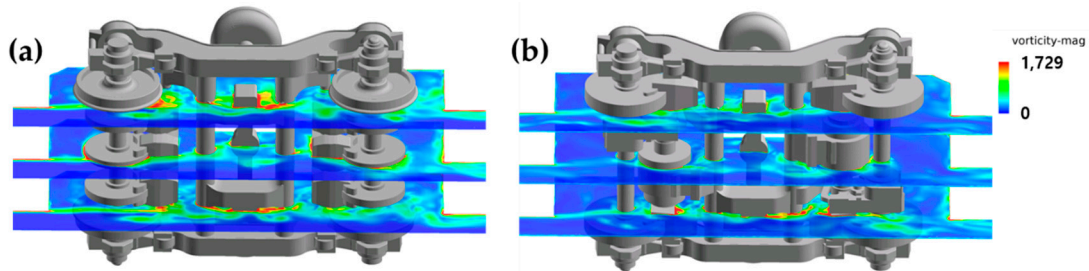


Figure 9. Instantaneous vorticity magnitude contours in  $x$ - $z$  plane at  $y = -0.6\text{m}, 0, 0.6\text{m}$ : (a) first bogie; (b) eighth bogie.

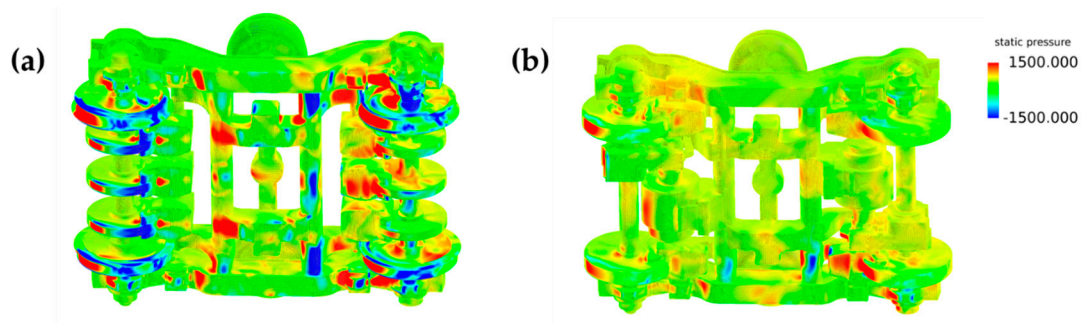


Figure 10. Instantaneous surface pressure contours: (a) first bogie; (b) eighth bogie.

The sound propagation pattern of which the center was located around the first bogie, shown in Figure 7a,b, manifested the strong aerodynamic source in the first bogie.

#### 4.3. Roof Fairing and Pantograph

Figure 11 shows the first and second pantographs, which consisted of a panhead, a lower arm, an upper arm, a base frame, and a driving device with pairings. The pantograph is well known to be one of main aerodynamic noise sources of a high-speed train because it is mounted on the train roof and exposed to the unsteady flows. Figure 12 shows the iso-contours of instantaneous vorticity magnitude on the vertical cross-sectional plane of the train. The significant flow separation on the roof was formed from the first and second pantographs, which can be also identified in Figure 5. Coherent vortices are generated around the first and second pantograph panheads, which generated the aerodynamic noise identified in Figure 7.

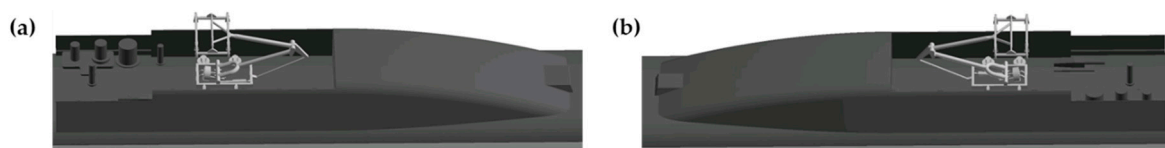
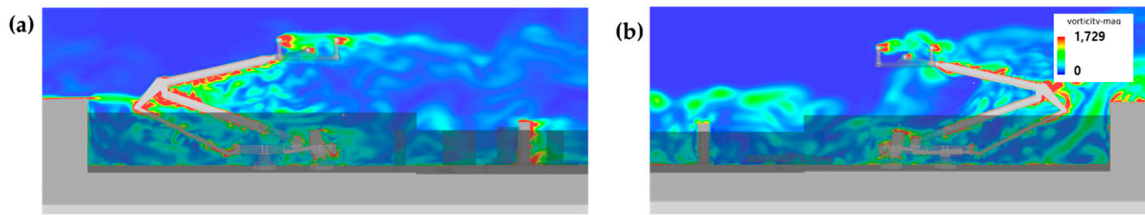


Figure 11. Simplified roof fairing and pantograph models: (a) first pantograph and roof pairing on the M1 car; (b) second pantograph and roof fairing on the M3 car.



**Figure 12.** Instantaneous vorticity magnitude contours on the  $x$ - $z$  plane at  $y = 0$  m: (a) first pantograph; (b) second pantograph.

#### 4.4. Intercoach Space

Intercoach space is one of the main noise sources of a high-speed train. Intercoach space can be categorized as an open cavity that has a large or small streamwise length-to-depth ratio [2]. In an open cavity which is also known to be aerodynamic noise source, the shear layer is separated from the leading edge of cavity and spans the entire length of cavity or roll-up to quasi-periodic vortices. The shear layer or vortices hit the solid rear wall of the cavity and generate aerodynamic noise by converting the vortical energy to acoustic energy.

The acoustic waves propagating upstream hit the leading edge of the cavity and enhance the development of the shear layer. This feedback phenomenon sometimes strengthens the aerodynamic noise by the resonance of its feedback frequency with the cavity acoustic modes. Figure 13 shows the iso-contours of instantaneous vorticity magnitude in intercoach regions. Typical shear-layer vortices in the wide-open cavity were identified in the upper part cavity, while the closed shear layers in the narrow open cavity were formed in the side part cavity of the intercoach space. Compared to the typical open cavity, however, the flow structure in the upper part of first intercoach space showed a more complex pattern. A strong shear layer was formed from the wind-shield and induced fluid flow from the inside cavity to the outside in the upper part of the cavity of the first intercoach region. Figure 14 shows the streamlines of fluid passing around the intercoach space. Heavy spiral flow was generated from the bogie side and rose to the roof side in the first intercoach space. On the other hand, spiral flows originated from the upper intercoach spaces in the second and third intercoaches. These complex vortices caused aerodynamic noise in the intercoaches, which was observed in Figure 7.

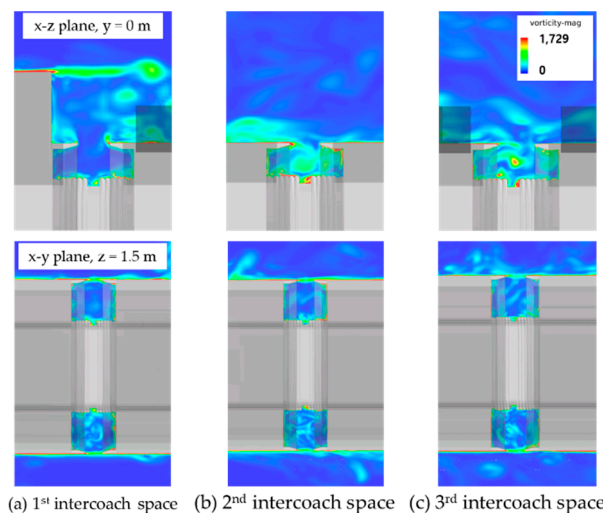


**Figure 13.** Instantaneous vorticity magnitude contours of intercoach regions at  $y = 0$  m.

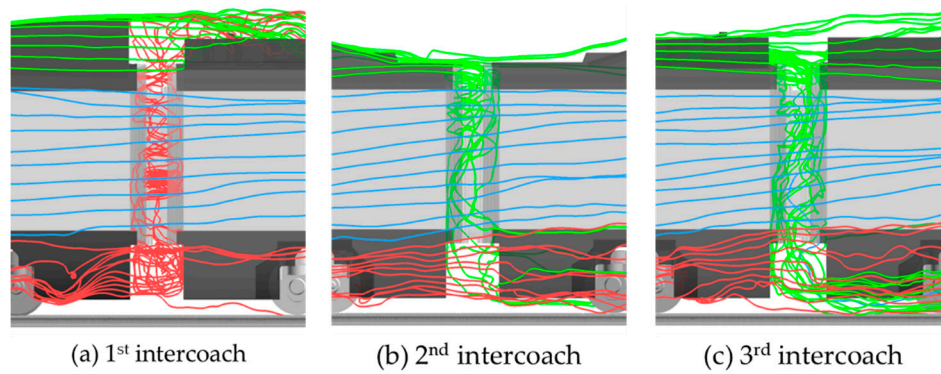


**Figure 14.** Streamlines near intercoach space: red: from bogie and bogie fairing; blue: from sidewall; green: from roof.

### 5. Decomposition of Surface Pressure

The illustrative wavenumber–frequency analysis was conducted by applying Equation (6) to the predicted surface pressure fields on the roof and the left-side wall surfaces of the TC car shown in Figure 15. The sampling rate  $f_s$  and the frequency interval  $\Delta f$  were 5000 Hz and 2.03 Hz, respectively. The wavenumber intervals  $\Delta k_x$  and  $\Delta k_z$  were 0.01954 (1/m) and 0.4379 (1/m), respectively. The power spectral density obtained from the wavenumber–frequency transform is plotted in Figure 16. The slanted Dirac cone ( $-c_0 + U_0 \leq \omega/k \leq c_0 + U_0$ ) was distinctly identified. To show the characteristics of the wavenumber–frequency diagram more clearly, the two-dimensional spectrum at the cross-sectional plane of  $k_y = 0$  and  $k_z = 0$  for the roof and left-side walls is shown in the right side of Figure 16. Strong compressible components were identified, between the characteristic lines of which the slopes corresponded to the phase speeds of  $|-c_0 + U_0| = 259.67$  m/s and  $|c_0 + U_0| = 426.33$  m/s, while most of the incompressible components were located on the line of slope  $U_c \cong 0.9U_0 = 75.00$  m/s.

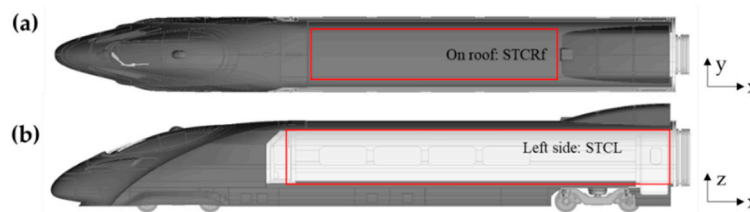


**Figure 15.** Surface regions of TC car for wavenumber–frequency analysis: (a) roof wall region; (b) left-side wall region.

These distinctly separated regions manifested that the LES simulation effectively captured the acoustic wave propagation as well as the aerodynamic noise generation in the external flow of the high-speed train. Figure 17a,b shows the power spectral density diagrams for the decomposed incompressible and compressible parts, respectively, and the corresponding power spectral density levels which were obtained by integrating the power spectral density over the entire wavenumber ranges in the form

$$S(\omega) = \int \int S(\mathbf{k}, \omega) dk_{x_1} k_{x_2} \tag{13}$$

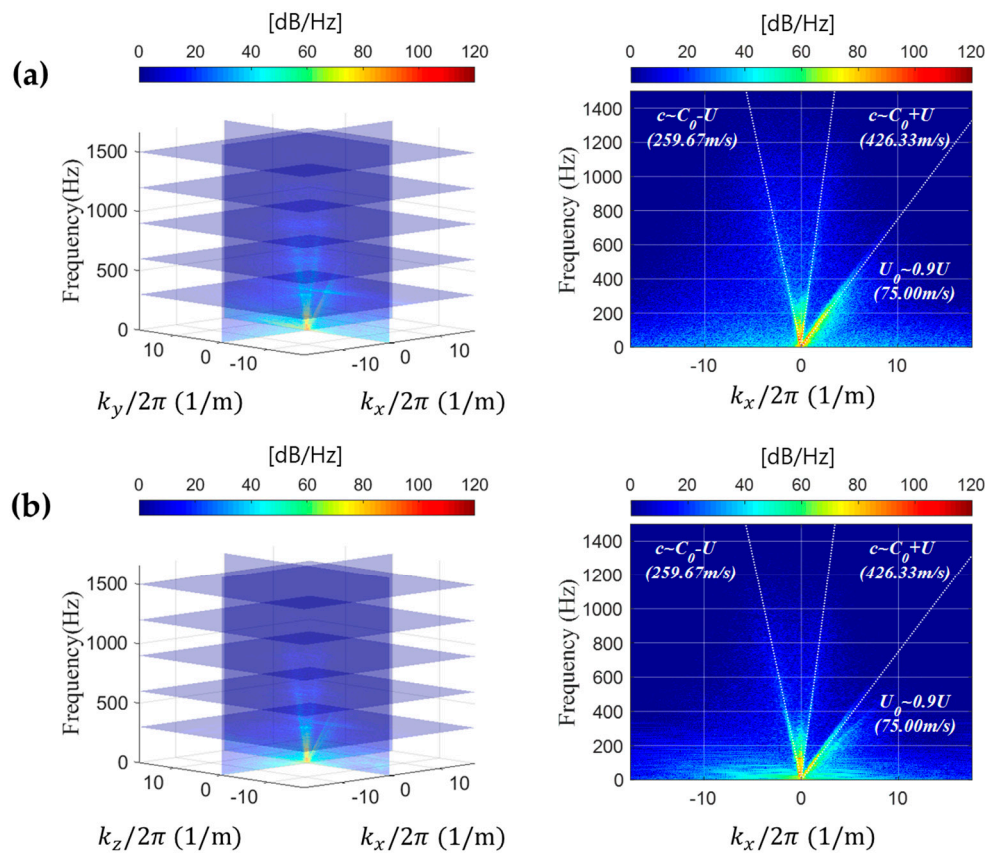


**Figure 16.** Three-dimensional power spectral density diagram (left) and diagrams at a given  $k_y = 0$  and  $k_z = 0$  (right)—reference pressure  $20 \mu\text{Pa}$ ; (a) roof wall region and (b) left-side wall region.

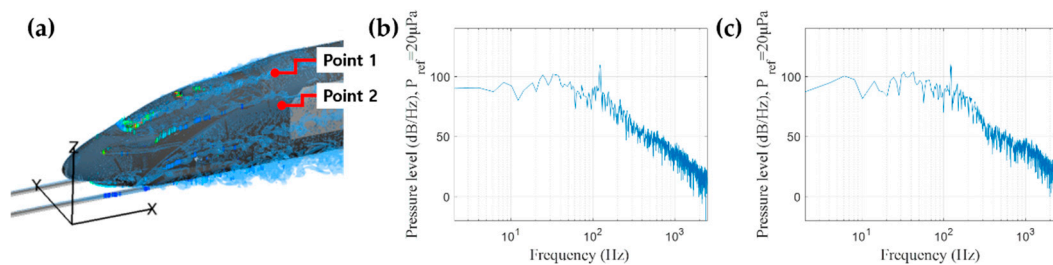


**Figure 17.** Pressure spectrum at Point 1 and Point 2: (a) locations of Point 1 and Point 2; (b) pressure spectrum at Point 1; (c) pressure spectrum at Point 2.

Equation (13) represents the averaged power spectral density levels of pressure over the surface regions shown in Figure 18. It can be seen that the incompressible pressure parts dominated in most of the frequency range, except for 120 Hz. This strong tonal component was caused by the coherent vortex shedding from the wiper, the headlamp, and first bogie fairing, as shown in Figure 17. The pressure spectrum obtained at the indicated locations showed the tonal peak at the frequency of 120 Hz.

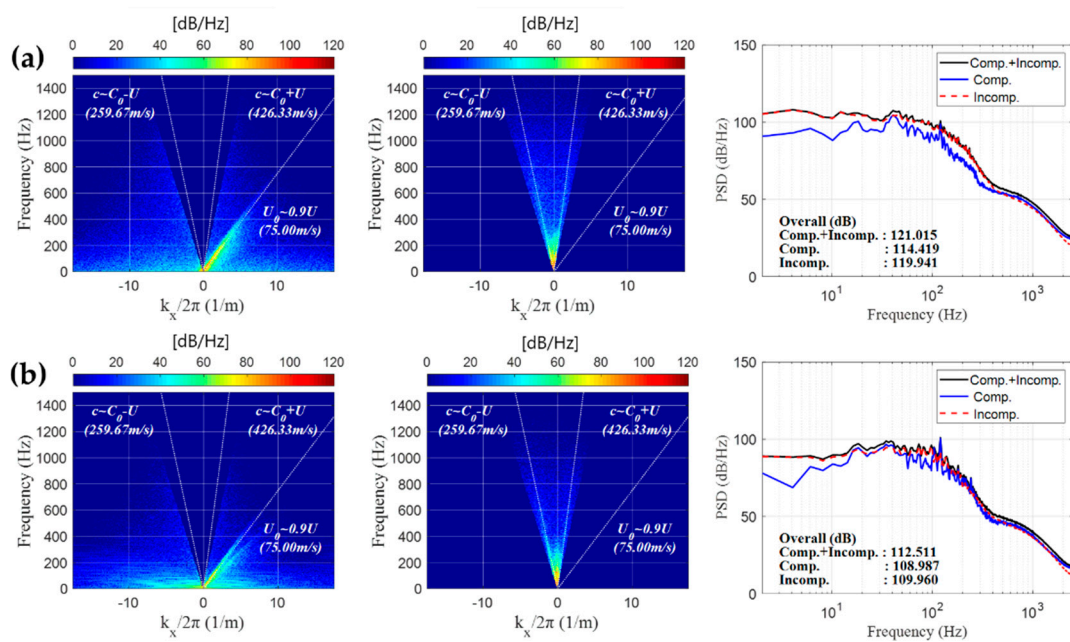


**Figure 18.** Decomposed power spectral density diagram of incompressible (left), compressible (middle) parts at a given  $k_y$ ,  $k_z = 0$  and power spectral density levels by integrating over all wavenumbers (right)—reference pressure 20  $\mu\text{Pa}$ : (a) roof wall region; (b) left-side wall region.

In order to obtain the compressible and incompressible surface pressure fields in the time-space domain, the inverse Fourier transform was taken for each separated region shown in Figure 18. Figure 19 shows the snapshot of incompressible and compressible surface pressure fields obtained in this way, together with the total pressure field for all coaches. It can be seen that the magnitudes of the incompressible components were generally much higher than those of the compressible ones, so that the total pressure field was almost similar to the incompressible pressure field. Although the magnitudes of compressible components were much lower, the present numerical method was able to extract the hidden acoustic pressure field successfully. It is well known that subsonic surface waves support an evanescent wave in a fluid which is always confined to the vicinity of the interface [11]. This fact implies that the acoustic pressure field with higher phase speed than the incompressible pressure field may make more contribution to the interior sound field of a high-speed train, which needs to be investigated in a future study.

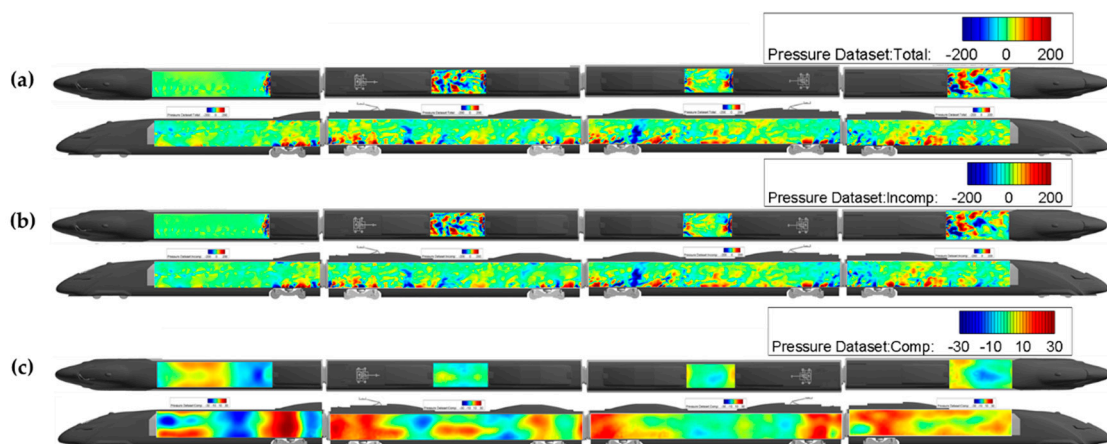


**Figure 19.** Decomposed instantaneous surface pressure field at time domain: (a) original total pressure field; (b) decomposed incompressible pressure field; (c) decomposed compressible pressure field.

The current wavenumber–frequency analysis was applied to the surface pressure fields on the roof and sidewall of all coaches. Table 4 summarizes the predicted overall power levels of total, incompressible, and compressible pressure fields. The highest total power levels were identified on the roofs of the M1 car and MC car, both of which were subjected to downstream flow behind the pantographs. The highest compressible pressure level was identified on the sidewall of TC car, which was directly exposed to the acoustic waves generated by the first bogie and the first intercoach space.

**Table 4.** Estimated overall power spectral density levels for each pressure field; unit: dB.

	TC Car		M1 Car		M4 Car		MC Car	
	Roof	Left Side						
Total	112.5	121.0	127.2	124.8	119.0	127.3	128.3	124.9
Comp.	109.0	114.4	109.7	111.6	105.2	112.7	111.2	111.9
Incomp.	110.0	120.0	127.1	124.6	118.8	127.2	128.2	124.7

## 6. Conclusions

In this study, the flow field around the high-speed train HEMU-430X running at the speed 300 km/h in an open field was computed by employing highly accurate large eddy simulation techniques with more than 300 million grid points. The predicted mean aerodynamic drag of the trains showed a good agreement with that reported in the available literature. The detailed analysis of the unsteady flow field identified three dominant aerodynamic noise source regions: the first bogie, the first pantograph, and the first intercoach space. In order to decompose surface pressure fluctuations into hydrodynamic and acoustic fluctuations, a wavenumber–frequency analysis was performed on the fluctuating surface pressure field on the train. The wavenumber–frequency diagrams of power spectral density showed two distinct regions corresponding to the hydrodynamic and the acoustic components of the surface pressure fluctuations. The application of inverse wavenumber–frequency transforms on each of the hydrodynamic and the acoustic components in the wavenumber–frequency domains successfully decomposed the surface pressure fluctuations into their incompressible and compressible parts in the time-space domains. The power spectrum levels of surface pressure were estimated for each coach’s surface. The sidewall surface of the TC car was found to be subject to the highest power level due to the compressible surface pressure field. To the best of authors’ knowledge, this is the first publication on the surface pressure power level due to compressible and incompressible pressure fields. The current results can be utilized to devise a useful measure for the reduction of interior cabin noise in high-speed trains.

A planned future study aims to incorporate the decomposed surface pressure fields for the prediction of the interior cabin noise of the high-speed train. The result will be utilized to assess the relative contributions of the incompressible and compressible surface pressure fields to the interior noise, and thus help to develop an effective cabin structure design for low interior noise.

**Author Contributions:** C.C. provided the basic idea for this study and the overall numerical strategies. S.L. carried out the numerical simulations and worked on the analysis of numerical results. J.K. and B.-h.K. provided the basic data of the HEMU-430X.

**Funding:** This research was supported by the Basic Science Research Program through the National Research Foundation of South Korea (NRF), funded by the Ministry of Education (NRF-2016R1D1A1A099 18456). This work was supported by ‘Human Resources Program in Energy Technology’ of the Korea Institute of Energy Technology Evaluation and Planning (KETEP), granted financial resource from the Ministry of Trade, Industry & Energy, Republic of Korea (no. 20164030201230).

**Conflicts of Interest:** The authors declare no conflict of interest.

## References

1. Thompson, D.J.; Iglesias, E.L.; Liu, X.; Zhu, J.; Hu, Z. Recent developments in the prediction and control of aerodynamic noise from high-speed trains. *Int. J. Rail Transp.* **2015**, *3*, 119–150. [[CrossRef](#)]

2. Zhu, J. Aerodynamic Noise of High-Speed Train Bogies. Ph.D. Thesis, University of Southampton, Southampton, UK, 2015.
3. Paradot, N.; Masson, E.; Poisson, F.; Grégoire, R.; Guilloteau, E.; Touil, H.; Sagaut, P. Aero-acoustic methods for high-speed train noise prediction. In Proceedings of the World Congress on Railway Research, Seoul, Korea, 18–22 May 2008.
4. Andreini, A.; Bianchini, C.; Facchini, B.; Giusti, A.; Bellini, D.; Chiti, F.; Federico, G. Large eddy simulation for train aerodynamic noise predictions. In Proceedings of the World Congress on Railway Research, Lille, France, 22–26 May 2011.
5. Yu, H.H.; Li, J.C.; Zhang, H.Q. On aerodynamic noises radiated by the pantograph system of high-speed trains. *Acta Mech. Sin.* **2013**, *29*, 399–410. [[CrossRef](#)]
6. Meskine, M.; Pérot, F.; Kim, M.; Freed, D.; Senthoooran, S.; Sugiyama, Z.; Polidoro, F.; Gautier, S. Community noise prediction of digital high speed train using LBM. In Proceedings of the 19th AIAA/CEAS Aeroacoustics Conference, Berlin, Germany, 24 May 2013.
7. Van Herpe, F.; Bordji, M.; Baresh, D.; Lafon, P. Wavenumber-frequency analysis of the wall pressure fluctuations in the wake of a car side mirror. In Proceedings of the 17th AIAA/CEAS Aeroacoustics Conference, Portland, OR, USA, 5–8 June 2011.
8. Lee, S.; Cheong, C. Decomposition of surface pressure fluctuations on vehicle side window into incompressible/compressible ones using wavenumber-frequency analysis. *Korean Soc. Noise Vib. Eng. (KSNVE)* **2016**, *26*, 765–773. [[CrossRef](#)]
9. Kwon, H. A study on the resistance force and the aerodynamic drag of Korean high-speed trains. *Veh. Syst. Dyn.* **2018**, *56*, 1250–1268. [[CrossRef](#)]
10. Thompson, D.J. *Railway Noise and Vibration: Mechanisms, Modelling and Means of Control*, 1st ed.; Elsevier: Oxford, UK, 2008.
11. Dowling, A.P.; Ffowcs Williams, J.E. Chapter 4.5: Evanescent waves. In *Sound and Sources of Sound*; Horwood E: Chichester, UK, 1983; pp. 90–93.



© 2019 by the authors. Licensee MDPI, Basel, Switzerland. This article is an open access article distributed under the terms and conditions of the Creative Commons Attribution (CC BY) license (<http://creativecommons.org/licenses/by/4.0/>).